Characterising the broadband, wide–angle reflectance properties of black silicon surfaces for photovoltaic applications

JACK J. TYSON,[*] [iD] **TUDOR E. SCHEUL, TASMIAT RAHMAN, AND STUART A. BODEN**

School of Electronics and Computer Science, University of Southampton, SO17 1BJ, UK
[*]*j.j.tyson@southampton.ac.uk*

Abstract: Black silicon nanotextures offer significant optical performance improvements when applied to crystalline silicon solar cells. Coupled with conventional pyramidal textures, to create so–called hybrid black silicon, these benefits are shown to be further enhanced. Presented here is a comprehensive analysis of different variations of this texture, coupled with typical anti–reflectance schemes such as coated pyramids, with a view to the significance of this on subsequent, real–world, solar energy generation. The study uses an angle–resolved spectrophometry system to characterise and compare the optical properties of these surface textures in terms of reflectance versus wavelength and incident angle, with and without encapsulant layers. This analysis, coupled with time-resolved, location specific irradiance data, leads to a new figure-of-merit, the weighted reflectivity, with which to compare surface textures for use in solar cells. Weighted reflectivity for an encapsulated solar cell surface, averaged over a year, for a Southampton, UK, location is calculated to be 7.6% for hybrid black silicon, compared to 10.6% for traditional random pyramids with a thin film anti–reflective coating.

1. Introduction

The nanoscale texturing of crystalline silicon (c-Si) solar cells, naturally dubbed 'black silicon' (b-Si) for its resultant appearance, has been subject to considerable research interest in recent years [1–4]. This is primarily due to the significant gains in optical performance offered with its use, with more light being absorbed into the substrate for subsequent electron-hole (e-h) pair generation. The methods used to create such textures vary from reactive ion etching (RIE) [5], to metal-assisted chemical etching (MACE) [6], and femtosecond laser (FsL) surface treatments [7]. For RIE and MACE methods, the resultant surface consists of vertically–aligned nanowires (NWs) with properties dependent on a large variety of factors including etch time, chemical composition, and temperature [8]. For FsL texturing, surface structure is dependent on pulse energy, duration, and angle of incidence [9,10]. The optical benefits of b-Si can be further enhanced when the texturing process is applied to microscale textures such as random pyramids [4] - a standard anti–reflectance texture used in monocrystalline silicon photovoltaics (PV). This combination of micron-scale pyramids decorated with nanoscale b-Si features is termed "hybrid b-Si" (hb-Si).

Black silicon does not interact with electromagnetic (EM) radiation in the same fashion as its microscale counterparts [11]. Pyramidal textures, for example, exhibit relatively good anti-reflectance arising from their ability to direct initially reflected light, that would otherwise be lost, onto adjacent facets for a second or third chance of being coupled into the solar cell. Furthermore, the redirection of light away from the normal means that reflected light escaping the surface is more likely to undergo total internal reflection at the overlying encapsulant interfaces

and be redirected back onto the cell. Light trapping within the cell is also enhanced by the texture as the inclined facets change the propagation direction of transmitted light through refraction, increasing the optical pathlength and therefore the amount of light absorbed. Pyramidal texturing is often combined with a thin film anti–reflection layer which operates through a destructive interference mechanism to further lower the reflectance of light at the silicon interface [12]. Nanoscale textures, such as b-Si, lead to a graded refractive index between the substrate and surrounding medium, smoothing the transition of light from one medium to the other and hence minimising reflectance over a broad spectral and angular range.

The measurement and quantification of optical performance for samples of applicability to solar PV is a crucial determinant in their effectiveness for use in such systems. We explore the application of MACE b-Si, applied to planar and pyramidal–textured substrates, and compare against the industry standard, microscale pyramids with a single–layer anti–reflectance coating. Optical performance is defined using front surface reflectance as measured with an in-house designed and constructed angle–resolved spectrophometry (ARS) system. A detailed description of the ARS can be found in our previous publication [13]. A new perception of these anti–reflectance schemes is showcased, enabling a more thorough analysis that includes variations in reflectance with both wavelength and angle of incidence. Other than simply observing the relation between the reflection from a surface of a solar cell and its angle dependency, it is shown that variable angle reflectance (VAR) data captured by the ARS can be related to the surface optical response to a moving source over time: the Sun [14]. Taking solar irradiance for a specific geographical location, and transient daylight hours for the same across a given year, the angle–dependant reflectance can be converted to to time– and seasonal–dependant reflectance, extrapolating anticipated optical performance of the surface design when it is applied to a PV cell. This leads to a single optical figure of merit; the weighted reflectivity (WR), which can be used to compare different anti–reflective schemes.

2. Experimental methodology

Four types of samples were fabricated for characterisation: a standard random pyramidal texture using an anisotropic potassium hydroxide (KOH) based chemical etch, the same with an 80 nm SiN_x single–layer ARC, several b-Si nanotextures of various heights using a MACE procedure [15,16], and hb-Si nanotextures, also of various heights, through a sequential series of KOH and MACE processes. The b-Si samples used here have etch times of 4, 6, 8, and 10 minutes, yielding mean NW heights of between 1.09 and 2.55 μm, respectively. As for the hb-Si samples, only the former three etch times were used, as a 10 minute MACE process on top of the random pyramids caused excessive deterioration of the microscale texture. The average heights of these hb-Si textured NWs for 4, 6, and 8 minute MACE were 0.79, 1.17, and 1.61 μm, respectively. Scanning electron micrographs of each textured sample can be seen in Fig. 1.

The ARS is used to perform high resolution centre–mount VAR scans on these nine samples, with a diffuse reflectance standard of 50% used as a reference. The ARS technical specifications and operational modes are outlined in [13], but the scan parameters used in this work were: $\lambda = 400 : 1000$ nm, $\theta = 8 : 80°$, where S– and P–polarisations were averaged together over five consecutive scans.

Subsequent to these measurements being taken, two of the best performing samples are then encapsulated in Norland Optical Adhesive (NOA) 61 [17] and 1.5 mm thick borosilicate glass. NOA 61 offers >95% transmission of light between wavelengths of 400 nm and 1.8 μm – covering the range of interest explored using the ARS system and completely covering the typical operating range of Si–based solar cells, and is a very close match to the performance of EVA, a commonly used adhesive in module production. The NOA 61 encapsulant layer is applied in the centre of each 3×3 cm sample, ensuring coverage does not exceed half the area of that sample. The borosilicate glass layer is then placed on top of this, causing the NOA 61
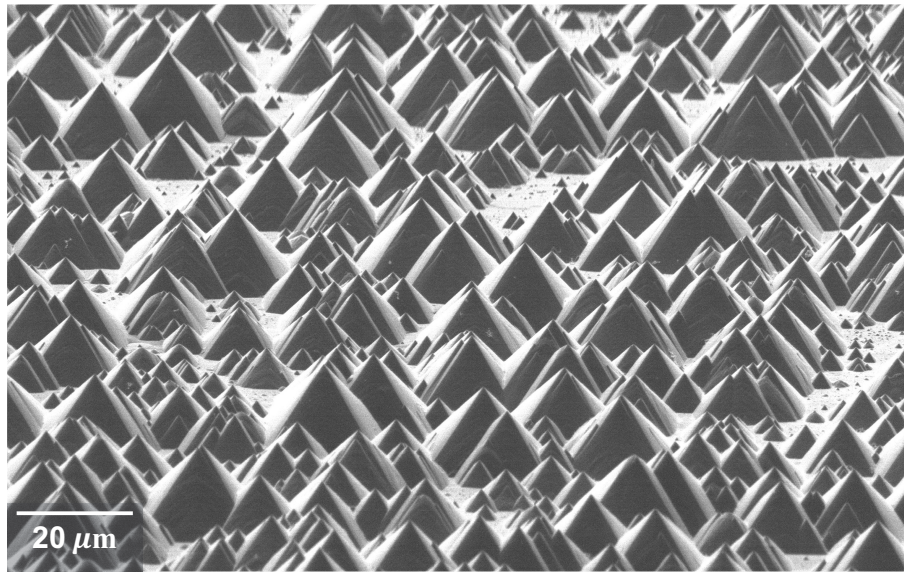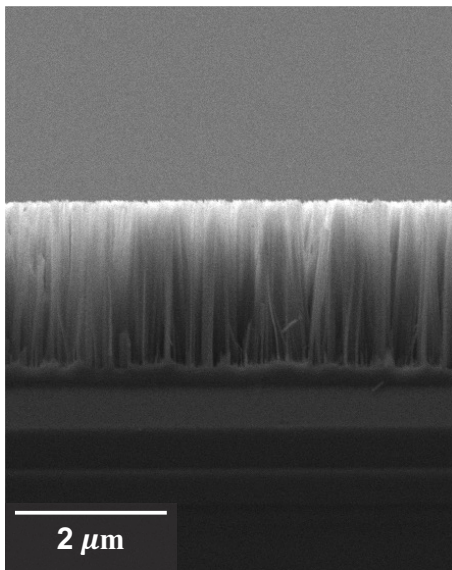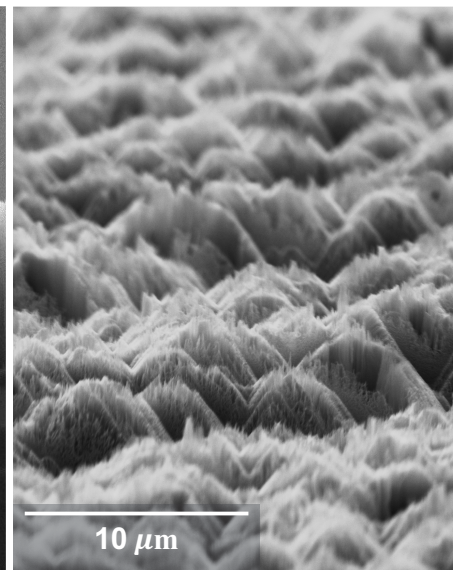
Fig. 1. Scanning electron micrographs of exemplar pyramidal (a), planar b-Si (b), and hb-Si (c) textures used in this work.

encapsulant to spread across the sample surface underneath the glass for complete surface area coverage. Samples were cured in an ultraviolet light irradiance box for a period of one minute, in–line with the manufacturer's specifications. Prior to completing any optical measurements, the encapsulated samples were inspected to confirm the absence of any visible air bubbles. It should be noted that this glass does not include its own ARC, and, as a result, front surface reflectance reported forthcoming for these samples may be slightly higher than those with this additional

glass ARC. Such a coating is common in production modules, and improves optical performance, but is not explored here.

3. Data analysis and methodology

In order to understand the process by which VAR data can be related to real–world equivalent scenarios, we first need to evaluate how the Sun moves relative to the solar panel over the length of the solar day, i.e. the proportion of a 24 hour period where the Sun is above the horizon. The solar day length is affected by several factors, such as specific geographical location, the height of the terrain above sea level (elevation), and whether the location is in the northern or southern hemisphere. The change in solar elevation throughout the year can be visualised by taking the two solstices (shortest and longest days of the year); all days in–between will have solar elevations situated between these two curves.

Solar elevation data is calculated using NREL's solar position algorithm (SPA) [18]. For this work, the parameters used in the SPA are tailored for Southampton, UK, having geographic coordinates of 50° 54′ 9.126″ N (latitude) and 1° 24′ 15.0804″ W (longitude), with an elevation of 2 m. Even when the Sun is below the horizon, light can still reach the solar panel indirectly. As such, negative values of elevation, that is to say when the Sun is below the horizon, are only included in situations whereby the SPA indicates a significant component of scattered light throughout the atmosphere. Month–dependent cloud coverage was included as part of this calculation, with coverage values provided by the Met Office [19] over a 10 year period.

Using spectral irradiance data, weighted average reflectance can be determined for a given sample. In typical, single angle reflectance measurement systems, this weighted average reflectance (WAR) is a single figure of merit weighted against the AM1.5G spectrum [20] to provide a more valuable insight into the true reflectance implications for solar PV technologies. WAR is determined for single angle reflectance as shown in Eq. (1), where R_x is the sample's surface reflectance, λ is wavelength, and $F_{AM1.5}$ is the AM1.5G spectral irradiance curve [20].

$$\text{WAR} = \frac{\int [R_x(\lambda) F_{AM1.5}(\lambda)] d\lambda}{\int [F_{AM1.5}(\lambda)] d\lambda} \tag{1}$$

In the case of variable angle reflectance, determination of a weighted reflectance must be done with respect to two variables simultaneously: wavelength and angle. Variable angle of incidence will require different irradiance spectra, F_{VAR}, to be weighted against, given the difference in air mass through which the light must pass before being incident on the surface of our samples. In this case, F_{VAR} can be determined using Bird and Hulstrom's Solar Irradiance Model [21,22]. This takes into account both direct and diffusely incident light and enables predictions of day–to–day optical performance of the anti–reflective surfaces, should they be employed in a real solar PV system. The definition of WAR, as in Eq. (1), can be expanded to include this angle–dependency of VAR measurements as shown in Eq. (2).

$$\text{WAR} = \frac{\int [R_x(\theta, \lambda) F_{VAR}(\theta, \lambda)] d\lambda}{\int [F_{VAR}(\theta, \lambda)] d\lambda} \tag{2}$$

The location of deployment for the model is Southampton, UK, where the panel is held at a fixed tilt of 35° from the horizontal and is south facing (as is optimal for use in the UK). Ozone levels are determined using the Heuklon model [23] and pressure is as typical at sea level (14.7 PSI). Direct light has an intensity linked directly to the angle of incidence, θ, meaning that it is only considered when the Sun is within the front facing hemisphere about the incident surface. When the Sun is either below the horizon, or illuminating the panel from behind, the direct illumination component is zero. Atmospheric scattering between these points, respectively,

causes some degree of indirect (diffuse) illumination. To account for this component, all non–zero values for diffuse irradiance over the course of the whole day, as determined using Bird and Hulstrom's Solar Irradiance Model [21,22], were averaged and divided through by the number of hours of direct irradiance for that day. This value could then be added to the values for direct irradiance, yielding total irradiance for the day as a whole. This allows for the inclusion of diffuse irradiance by assuming even distribution across the angular range.

It should be noted that the minimum direct solar elevation angle is always zero. The only situation when this is an incorrect statement is at either of the poles, where the Sun can remain below or above the horizon for months at a time. The solar elevation angle alone cannot be linked directly to the angle of incidence measured using the ARS. The angles present in the VAR contour plots are relative to the surface normal for that sample. For example, when light from the Sun is incident on the panel parallel to the surface normal, this relates to an ARS angle of $0°$. The angular distribution of our scans are limited to between 8 and $80°$. In order to ensure full spectral coverage in the theoretical determination of performance on a solar panel, this range needs to go from the minimum to maximum possible angles of incidence (0 and $90°$, respectively). This is readily achieved through the careful extrapolation of our VAR data. When light approaches any sample at an angle tending toward $90°$ relative to the surface normal, reflectance will tend toward unity. Meanwhile, at angles close to normal incidence, data has shown that reflectance is typically only wavelength dependent; changes to angle of incidence do not significantly change the reflectance measured at a given wavelength. This means that the VAR data can be extended from the original distribution of 8 to $80°$ to between 0 and $90°$ whilst maintaining validity by assuming spectral reflectance is the same for all values of θ below $8°$ ($R_x(0 \leq \theta < 8°, \lambda) = R_x(\theta = 8°, \lambda)$), and also assuming reflectance increases linearly towards 100% for all values of θ above $80°$ ($\lim_{\theta \to 90°} R_x(\theta, \lambda) = 1$). Here, R_x is the sample's surface reflectance, θ represents angle of incidence (with respect to the surface normal), and λ is wavelength.

Spectral irradiance data was calculated for each hour of the day, across every day of the month, over every month of the year. Each of these spectra were averaged with their counterparts from the same month, creating an average solar day indicative of that month. This average day can then be taken to assess the optical performance of our samples for each daylight hour in said day, yielding a number of data points representing expected optical performance for a typical day within each month of the year. WR is a single optical figure of merit, weighted against solar irradiance, for each month of the year, representing the average response across that month. This can also be averaged across a larger timescale, for example the whole year, to determine the same over a given year for a specific location.

4. Results and analysis

4.1. Samples prior to encapsulation

4.1.1. Pyramidal textures

As is expected, bare, uncoated pyramids perform relatively poorly. Figure 2(a) shows how the pyramidal structures maintain an almost linearly-increasing reflectance over increasing angles. The point of lowest reflectance lies between 600 and 750 nm at the minimum angle ($8°$), where the reflectance drops to approximately 11.7%. The reflectance peaks at 30% at high angles of incidence in the near infra-red (NIR) and near ultra-violet (NUV) spectral regions, but holds slightly lower at around 25% in the visible. In reference to Fig. 2(b), when a 80 nm thin film coating of SiNx is applied to the same pyramids, the reflectance minima shifts considerably into the visible spectrum at a wavelength of approximately 550 nm. The reflectance minima at $8°$ is only 1.35%, a mere $\sim 15\%$ of the minima seen in Fig. 2(a) for uncoated pyramids when we ignore the wavelength shift. Taking the reflectance of the uncoated pyramids at 550 nm (not

the minima for that sample), the reflectance of the ARC coated sample is approximately 10% that prior – a considerable optical performance boost. Furthermore, the minima for the sample shown in Fig. 2(b) does not shift up or down the wavelength spectrum, remaining almost constant throughout the angular distribution.

(a)   (b)
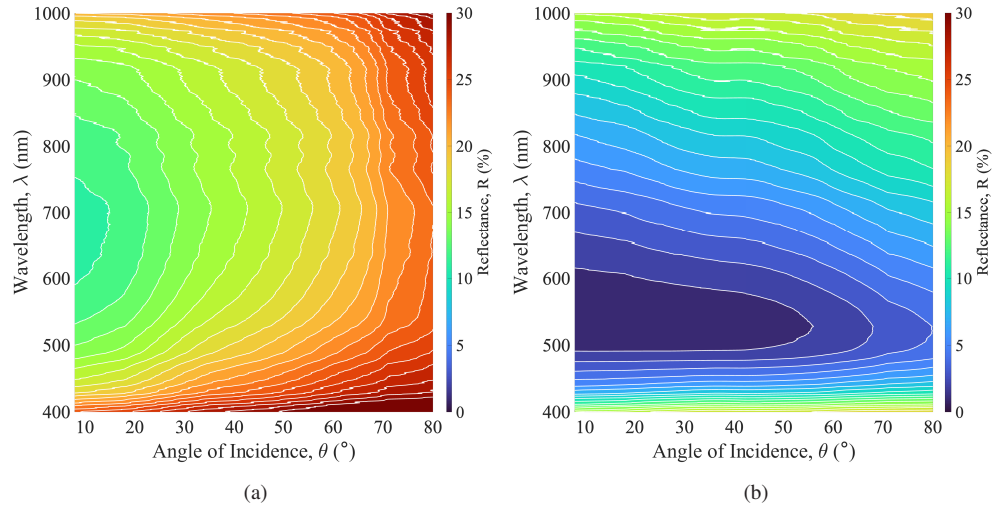
Fig. 2. The VAR data for uncoated pyramidal samples (a), and pyramidal samples with an 80 nm SiNx ARC (b).

4.1.2. Black silicon and hybrids

The ARS data for planar b-Si textures, which can be seen in Fig. 3, reveals that there is a noticeable difference between the optical response when compared to either of the pyramid–based textures in Figs. 2(a) and 2(b). A combination of both vertical and horizontal lines, applicable in different areas of the wavelength and angular distribution, demonstrates wavelength or angle independence that in itself is dependant on both of these properties. For example, reflectance can be seen to remain constant regardless of incidence angle up to between 40° and 60°, with the latter applicable for wavelengths in the NIR and NUV, and the former for the visible spectrum. A distinct rectangular pattern is created by this characteristic for a subset within the reflectance data, for each of the etch times shown, but with greater prominence for $t_e > 4$ minutes (Figs. 3(b), 3(c), and 3(d)). In the case of $t_e = 4$ minutes (Fig. 3(a)), this feature is slightly more obscured but still remains visible through higher values of reflectance.

Crucial to note, in the case of all samples as in Fig. 3, reflectance in the visible spectrum, $400 \leq \lambda \leq 700$ nm, is consistently the lowest throughout the angular sweep, holding even up to very high incidence angles of 80°. Reflectance for these samples is, in terms of absolute reflectance, generally 5 to 10% higher than the visible region in the NIR above 60°.

For longer etch times, and thus taller NWs, the low reflectance contour regions can be seen to grow and expand to fill the VAR data plots. Nanostructured b-Si surfaces create a graded refractive index effect between the superstrate (air) and substrate (Si). The taller the NWs are the shallower this gradient is, resulting in a smoother transition between the two media, and hence a better anti–reflective effect. This is why longer etch times produce b-Si surfaces with decreasing levels of reflectance.

The reflectance minimum for the 4 minute sample represented in Fig. 3(a) is located at approximately 500 nm and shifts toward 650 nm suddenly about an incidence angle of 60°. The reflectance at these points is 3.8% and 18.9%, respectively. As the etch time is increased through
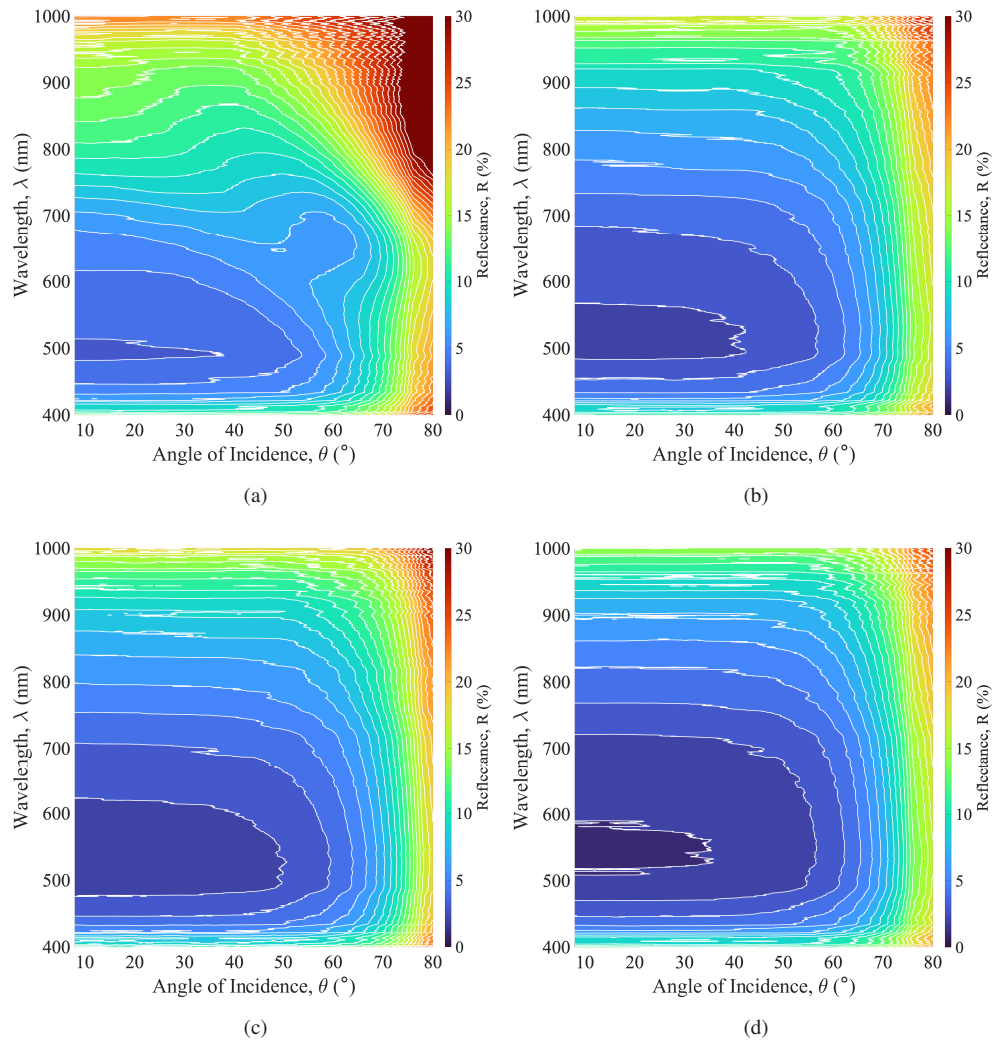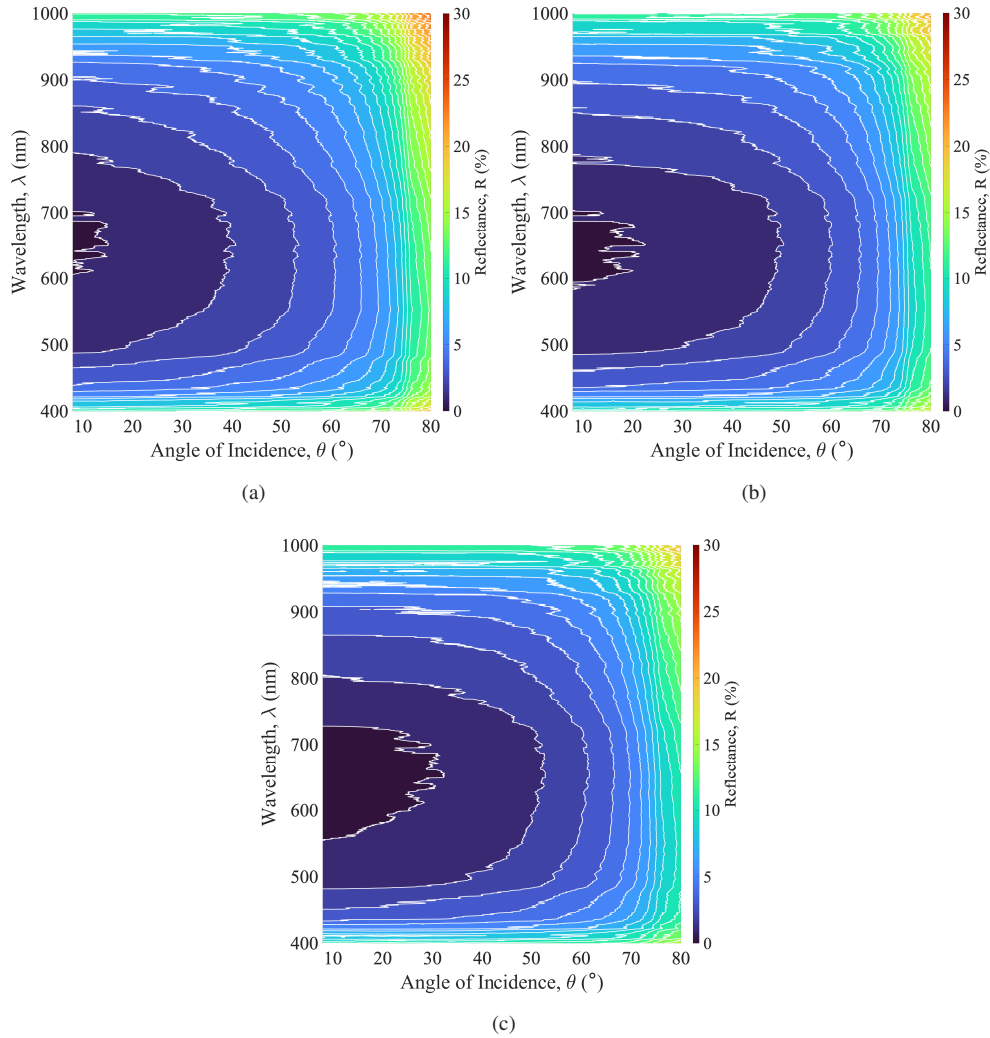
Fig. 3. The VAR data for our b-Si samples for etch times of 4 (a), 6 (b), 8 (c), and 10 (d) minutes.

to 10 minutes, this minima shifts upward toward 550 nm but remains in position regardless of incidence angle.

The maximum reflectance, sample irrespective, is at 80° and in the NIR – the top right corner of each contour plot. This is mirrored in the NUV, where Si is highly reflective by default. Planar b-Si surface texturing can be seen to make significantly better use of the NIR and NUV when compared to pyramids inclusive of an ARC. On comparison of Figs. 2(b) and 3, the low reflectance region of the pyramid–based sample stretches to the right, however the same region for b-Si is instead stretched diagonally upwards to the right, permitting a far greater area coverage outside the visible spectrum. Despite this, the data in Fig. 2(b) does show how pyramids, when coupled with an ARC, can outperform b-Si in terms of minimum reflectance levels. In order for b-Si to reach an equivalent level of reflectance, the NWs would need to be excessively tall – a hindrance for solar applications given the increasing complexity of passivating a surface with disproportionate features (far taller structures than they are wide, for example).

Fig. 4. The VAR data for our hb-Si samples for etch times of 4 (a), 6 (b), and 8 (c) minutes.

As we move to hb-Si textures, there is once again a clear jump in optical performance across the spectrum. Figure 4 shows the data for hb-Si samples etched using the MACE process for periods of 4, 6, and 8 minutes. Immediately apparent is the shift in minima between 500 and 550 nm for planar b-Si, to ~ 650 nm in the case hb-Si.

On taking the worst performing hb-Si sample (t_e = 4 minutes), the substantially lower reflectance minima at both 8° and 80° when compared to even the best performing b-Si sample (t_e = 12 minutes) is clear. At 8°, the 4 minute hb-Si sample has less than 50% the reflectance of the 12 minute b-Si sample. Notably, the wavelength position of the reflectance minima at shallow angles of incidence remains the same between all the datasets in Fig. 4. Moreover, the hb-Si samples are shown to exhibit a broader anti–reflective effect over both wavelength and angle ranges compared to the planar b-Si samples.

Surface passivation, usually through the deposition of a thin film of a dielectric material, is essential for solar cells to function effectively. However, the introduction of nanoscale surface texturing can hinder the application of a uniform passivation layer across the entire surface, as is
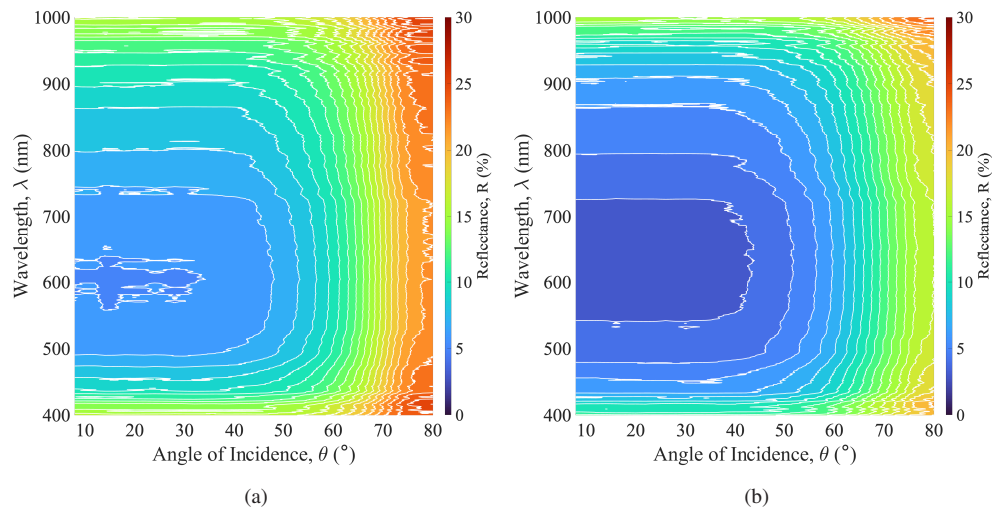
Fig. 5. The VAR data for the pyramidal sample with an 80 nm SiNx ARC (a) as well as the 4 minute hb-Si sample (b), now encapsulated.

required for high performance. The deposition of a passivation layer, in the case of b-Si or hb-Si, needs to result in conformal coverage of each individual NW. This is possible through atomic layer deposition methods [3,4], but is increasingly more difficult to achieve the taller and more complex the texture features are. The results in Fig. 4 show that there is only a small decrease in reflectance for increasing NW height for the hb-Si samples, in contrast to the larger decreases in reflectance seen for the equivalent b-Si samples. As such, it is possible to compromise on overall reflectance and select the hb-Si sample with shorter NWs for application onto a solar cell, whilst still maintaining exceptional levels of optical performance and good compatibility with existing passivation methods.

4.2. Samples after encapsulation

On applying an encapsulant (NOA 61) layer and glass (borosilicate) layer to the samples, the VAR characteristics of the samples fundamentally change to correspond with what would be expected for real–world deployment. It is assumed that the electrical contacts would be mounted on the rear of the cell (that is to say an IBC) to ignore any self–shading effects. The updated VAR contours for the two encapsulated samples can be seen in Fig. 5.

The general patterns for both textures in Fig. 5 are more consistent with one another than shown in previous plots without the inclusion of any encapsulant layers. Take the pyramids inclusive of the single–layer ARC, for example. When unencapsulated (Fig.. 2(b)), this texture exhibits a distinct low–reflectance band formed along the angular distribution between wavelength of 500 and 600 nm, extending all the way up to an 80° incidence angle. When encapsulated (Fig. 5(a)), the reflectance contours form a pattern similar to that of the hb-Si, and the uncoated pyramids as seen in Fig. 2(a). Data compared from each of these Figs. (2(a), 2(b), and 5), as well as Fig. 4, suggests that similar base structures, in this case pyramids, illicit similar spectral reflectance curves under the same incident lighting conditions, whereby the magnitude of reflectance is dictated by the coating (if any) applied to such structures.

Both textures, as to be expected, exhibit increased reflectance minimum resulting from the greater number of optical interfaces present. Each interface, according to the Fresnel equations, will both transmit and reflect a certain quantity of light. There will also be loss resulting from absorption in the encapsulant layers, reducing the total energy available for e-h pair generation.

The VAR reflectance minima for the hb-Si and pyramidal samples shown in Fig. 5 are 3.7% and 5.9%, respectively. This represents an increase of 3% and 4.6%, respectively. Reflectance levels in the NUV and NIR are noticeably lower for the sample shown in Fig. 5(a) when compared to the same sample without encapsulation. This apparent optical improvement is due to the increased refractive index steps between the air and silicon that help to steer the light inward toward the normal through refraction. Pyramids see the biggest improvement in these spectral regions as their ARC topography does not create the graded refractive index seen with nanostructures like Si NWs.

Conformity between the NOA 61 encapsulant and surface texturing is an influential factor on optical performance requiring discussion. Typically, microscale textures such as pyramids allow the encapsulant layer, applied as a liquid, to conformally coat the Si substrate surface with no trapped air bubbles. However, nanoscale textures like the hb-Si structures, with very small gaps between each nanowire or nanowire cluster, make it difficult for the encapsulant to conform well to the Si material. As a result of the viscosity of NOA 61, coupled with the nanoscale pores exhibited by hb-Si, it is likely that the encapsulant is unable to seep into these gaps – instead simply sitting on top of the NW structures. This creates pockets of air situated between the encapsulant, NWs, and substrate surface, affecting the smooth graded refractive index seen previously and will contribute to the measured reflectance for such samples.

4.3. Weighted reflectance

The pyramids featuring an 80 nm layer of SiNx and the 4 minute hb-Si sample are carried forward for further analysis. For reference, the average height of the NWs on the 4 minute hb-Si samples is 790 nm. The WR for the samples shown in Figs. 2(b) and 4(a) can be seen in Fig. 6 as a function of the month in the year. For both anti–reflective surfaces, it can be seen that WR is higher in the winter months. This is to be expected given the lower average elevation of the Sun during winter. At and around the winter solstice, the Sun maintains a far lower elevation, and thus a larger angle with the surface normal, for the majority of the solar day. By contrast, the Sun is much higher in the sky throughout the summer months, resulting in a smaller angle of incidence and hence a lower reflectance.

The sample consisting of pyramids with an ARC coating, a standard for c-Si solar PV, performs well and consistently throughout the year. At its worst, this scheme exhibits a WR of approximately 15.9%. This drops down to a value of just 8.8% in the high–elevation summer months, with the best performing month being June. The mean WR across the entire year is 10.6%. On the other hand, hb-Si performance varies more than the pyramids, starting only slightly lower in winter and swinging much lower in the summer. The WR for hb-Si ranges between 15.4% and 4.8% over the year, with an average WR of 7.6%. This shows the hb-Si surface as the best overall performer, with significant performance improvements over conventional texturing in the summer months, and slightly better relative performance in the winter months. This data showcases points made previously, whereby weighted average reflectance measurements are crucial to *fully* understanding the implications of solar cells, particularly those with nanoscale texturing that behave very differently to their microscale counterparts under incident illumination.

Re–evaluating the WR for encapsulated samples brings a considerable change in theoretical performance when located in Southampton. Figure 6 shows how peak performance, once again, can be obtained during peak summer usage with the longest days, and highest solar elevation. However, optical losses are much higher than in the absence of encapsulation. The lowest WR for these samples are 8.1% and 9.9% for hb-Si and coated pyramids, respectively. It is once again highest in the winter months, hitting highs of 19.4% and 22.6%, respectively, with average weighted reflectivities of 11.6% and 14%. These key statistical points for the WR presented in Fig. 6 are summarised in Table 1 for reference. This figure, coincidentally, showcases the advantage of hybrid structures when used over the whole year, with a consistently better
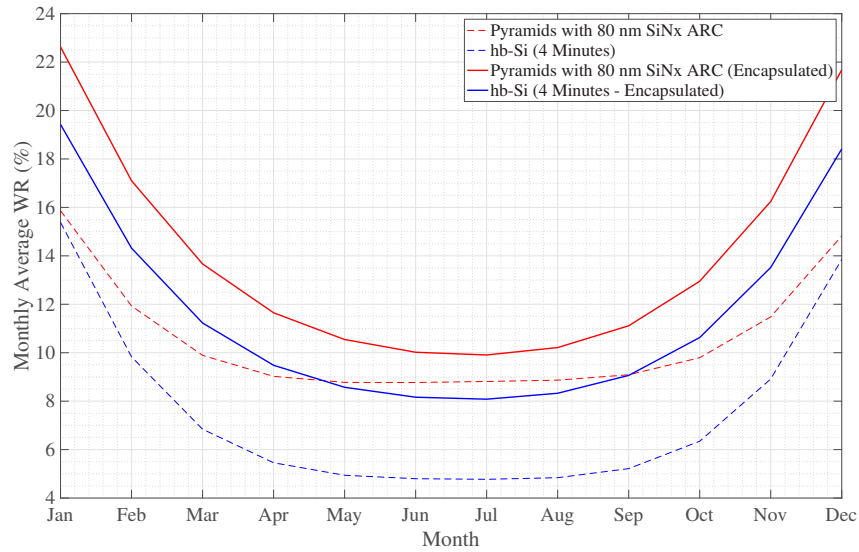
Fig. 6. The monthly average WR determined for both pyramidal (red) and hb-Si (blue) samples, with VAR as shown in Figs. 5(a) and 5(b), respectively. The data shown here is for Southampton, UK.

performance across every month of the year. When encapsulated, the shape of both WR curves become very similar, with only an apparent translational difference along the *y*–axis. This is subtly different to when the samples were unencapsulated, where the curves have slightly differing shapes to one another.

Table 1. An overview of the key data statistics for the samples shown in Fig. 6.

Sample	Monthly Av. WR (%)		
	Min.	*Max.*	*Mean*
Pyramids + 80 nm SiNx ARC	8.8%	15.9%	10.6%
Pyramids + 80 nm SiNx ARC (Encapsulated)	9.9%	22.6%	14%
hb-Si	4.8%	15.4%	7.6%
hb-Si (Encapsulated)	8.1%	19.4%	11.6%

5. Conclusions

We have employed the versatility of the ARS for angle–resolved reflectance measurements on several nanoscale textures such as b-Si and hb-Si, alongside traditional anti–reflectance mechanisms such as microscale pyramidal textures that are both bare and coated with an ARC. We also apply theoretical calculations to extrapolate the performance of these anti–reflectance methodologies should they be applied to all back contacted silicon solar cells inclusive of their encapsulation and glass layers. Bare pyramids are initially used as the baseline sample, with every subsequent sample outperforming it. The VAR performance of b-Si generally sat behind that of the coated pyramids, with the only exception being the longest etch time of 10 minutes, which equated to NWs with an average height of 2.55 μm. This optical efficiency is visibly proportional to NW height as a result of the gradient in refractive index created by these nanostructures. A similar effect could be seen with hb-Si samples that comprised of longer NWs; reflectance

steadily decreased with increasing NW height, but to a far smaller degree than planar b-Si due to the already substantially low levels of reflectance.

Consideration was made regarding the applicability of these textures to solar applications. Excessive NW height makes these surfaces difficult to passivate effectively – a considerable drawback to the approach. In finding the appropriate balance between height and optical performance, we selected the hybrids containing NWs under 1 μm, being the 4 minute etch. This decision was supported by literature on the subject as well as the optical performance quantified in Fig. 4(a). This hybrid black silicon sample was carried forward to be compared with its primary competitor: pyramids coated with an ARC.

When encapsulant and glass layers were applied and the VAR and WR analyses were re–run, hb-Si was shown to be highly effective and performed better than its pyramidal counterpart. WR ranged from 8.1% to 19.4% over the year. In comparison, the WR of pyramids inclusive of these encapsulant and glass layers varied from 9.9% to 22.6% under the same conditions. Hb-Si textures are shown to perform notably better than pyramids with NIR and NUV responses considerably lower when unencapsulated. This difference in performance is still present but notably less when both are encapsulated, where the encapsulant layers reduce the angular range of incident light through refraction towards the normal.

This work demonstrates how obtaining the full spectral and angular reflectance characteristics of a surface can be used to compare anti–reflective schemes for applications where broadband light is incident at varying angles, using crystalline silicon photovoltaics as an example. The approach is extendable to other photovoltaic technologies and to other applications in optics for which the illumination conditions change over time.

Disclosures. The authors declare no conflicts of interest.

Data availability. Data underlying the results presented in this paper are available in Ref. [24].

References

1. S. K. Srivastava, D. Kumar, P. K. Singh, and V. Kumar, "Silicon nanowire arrays based "black silicon" solar cells," in *2009 34th IEEE Photovoltaic Specialists Conference (PVSC)*, (IEEE, 2009).
2. S.-C. Shiu, S.-B. Lin, and C.-F. Lin, "Reducing Si reflectance by improving density and uniformity of Si nanowires fabricated by metal-assisted etching," in *Conference on Lasers and Electro-Optics 2010*, (OSA, 2010).
3. H. Savin, P. Repo, G. von Gastrow, P. Ortega, E. Calle, M. Garín, and R. Alcubilla, "Black silicon solar cells with interdigitated back-contacts achieve 22.1% efficiency," Nat. Nanotechnol. **10**(7), 624–628 (2015).
4. T. Rahman, R. S. Bonilla, A. Nawabjan, P. R. Wilshaw, and S. A. Boden, "Passivation of all-angle black surfaces for silicon solar cells," Sol. Energy Mater. Sol. Cells **160**, 444–453 (2017).
5. S. Grigoropoulos, "Highly anisotropic silicon reactive ion etching for nanofabrication using mixtures of SF$_6$/CHF$_3$ gases," J. Vac. Sci. Technol., B: Microelectron. Nanometer Struct.–Process., Meas., Phenom. **15**(3), 640–645 (1997).
6. A. G. Nassiopoulou, V. Gianneta, and C. Katsogridakis, "Si nanowires by a single-step metal-assisted chemical etching process on lithographically defined areas: formation kinetics," Nanoscale Res. Lett. **6**(1), 597 (2011).
7. A. Y. Vorobyev and C. Guo, "Antireflection effect of femtosecond laser-induced periodic surface structures on silicon," Opt. Express **19**(S5), A1031 (2011).
8. H. Omar, M. J. Salifairus, S. A. H. Alrokayan, H. A. Khan, A. M. M. Jani, M. Rusop, and S. Abdullah, "Effect of temperature to the structure of silicon nanowires growth by metal-assisted chemical etching," in *2015 IEEE Student Conference on Research and Development (SCOReD)*, (IEEE, 2015).
9. T.-H. Her, R. J. Finlay, C. Wu, and E. Mazur, "Femtosecond laser-induced formation of spikes on silicon," Appl. Phys. A: Mater. Sci. Process. **70**(4), 383–385 (2000).
10. C. H. Crouch, J. E. Carey, J. M. Warrender, M. J. Aziz, E. Mazur, and F. Y. Génin, "Comparison of structure and properties of femtosecond and nanosecond laser-structured silicon," Appl. Phys. Lett. **84**(11), 1850–1852 (2004).
11. M. W. Amdemeskel, C. Dam-Hansen, B. Iandolo, R. S. Davidsen, O. Hansen, G. A. dos Reis Benatto, N. Riedel, P. B. Poulsen, S. Thorsteinsson, and A. Thorseth, "Indoor measurement of angle resolved light absorption by black silicon," in *2017 IEEE 44th Photovoltaic Specialist Conference (PVSC)*, (IEEE, 2017).
12. S. A. Boden and D. M. Bagnall, "Sunrise to sunset optimization of thin film antireflective coatings for encapsulated, planar silicon solar cells," Prog. Photovolt: Res. Appl. **17**(4), 241–252 (2009).
13. J. J. Tyson, T. Rahman, and S. A. Boden, "Angle–resolved spectrophotometry for the optical characterisation of material surfaces," IEEE Trans. Instrum. Meas. **71**, 1–8 (2022).

14. J. J. Tyson, T. Rahman, and S. A. Boden, "Analysing the optical performance of hybrid black silicon surface textures under variable angle illumination," in *SuperSolar Annual Conference 2022*, (2022).

15. T. E. Scheul, E. Khorani, T. Rahman, M. D. Charlton, and S. A. Boden, "Wavelength and angle resolved reflectance measurements of pyramidal textures for crystalline silicon photovoltaics," Prog. Photovolt: Res. Appl. **28**, 1248–1257 (2020).

16. T. E. Scheul, "Metal-assisted chemically etched black silicon: morphology and light interaction," Ph.D. thesis, University of Southampton (2020).

17. Norland Products, "Norland optical adhesive 61," (2022).

18. I. Reda and A. Andreas, "Solar position algorithm for solar radiation applications," Sol. Energy **76**(5), 577–589 (2004).

19. "Gridded datasets of monthly values – mean cloud cover (%)," resreport, Met Office (2011).

20. "Tables for reference solar spectral irradiances: Direct normal and hemispherical on 37 tilted surface,".

21. R. E. Bird and R. L. Hulstrom, "A simplified clear sky model for direct and diffuse insolation on horizontal surfaces," Tech. rep., Solar Energy Research Institute (1981).

22. R. E. Bird and C. Riordan, "Simple solar spectral model for direct and diffuse irradiance on horizontal and tilted planes at the Earth's surface for cloudless atmospheres," Tech. rep., Solar Energy Research Institute (1984).

23. T. K. Van Heuklon, "Estimating atmospheric ozone for solar radiation models," Sol. Energy **22**(1), 63–68 (1979).

24. J. J. Tyson, "Dataset: Characterising the broadband, wide–angle reflectance properties of black silicon surfaces for solar photovoltaic applications," (2023).